Journal of Hazardous Materials 389 (2020) 122150

Contents lists available at ScienceDirect

Journal of Hazardous Materials

journal homepage: www.elsevier.com/locate/jhazmat

Natural fluorapatite dissolution kinetics and Mn^{2+} and Cr^{3+} metal removal from sulfate fluids at 35 °C

Veerle Vandeginste[a,b,*], Charlotte Cowan[a], Rachel L. Gomes[c], Tharwat Hassan[a], Jeremy Titman[a]

[a] School of Chemistry, University of Nottingham, University Park, Nottingham, NG7 2RD, United Kingdom
[b] GeoEnergy Research Centre, University of Nottingham, University Park, Nottingham, NG7 2RD, United Kingdom
[c] Department of Chemical and Environmental Engineering, Faculty of Engineering, University of Nottingham, University Park, Nottingham, NG7 2RD, United Kingdom

GRAPHICAL ABSTRACT

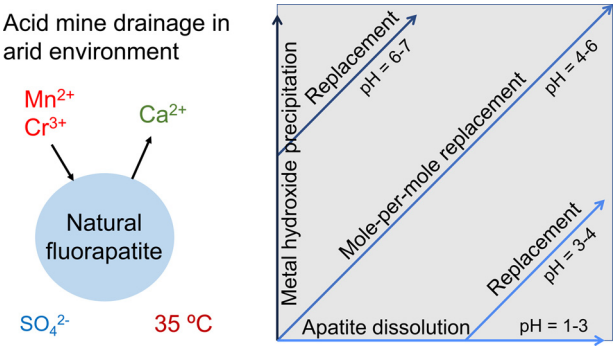

ARTICLE INFO

Editor: Navid B Saleh

Keywords:
Apatite
Heavy metals
Dissolution and precipitation
Removal efficiency
Acid mine drainage
Arid

ABSTRACT

In light of the consequences of global warming and population growth, access to safe drinking water becomes an ever greater challenge, in particular in low to middle income countries in arid regions. Moreover, mining which may cause acid mine drainage and heavy metal contamination puts further pressure on management of limited water resources. Hence, the development of cost effective water treatment methods is critical. Here, using batch reactor experiments we investigate the kinetics and mechanisms behind divalent Mn and trivalent Cr removal from sulfate fluids using natural fluorapatite at 35 °C. The results show that the fluorapatite dissolution rate depends on fluid pH, and that dissolution is the dominant mechanism in fluids with pH below 4. Apatite can thus serve as remediation to neutralize acidic fluids. Fluid pH of 4–6 triggers a dissolution-precipitation mechanism, in some cases following upon a dissolution-only period, with the formation of a metal phosphate. In these experiments, Cr removal is two to ten times faster than Mn removal given similar solution pH. The results demonstrate that natural apatite represents a promising, cost effective material for use in passive remediation of mining-induced contamination of soils and groundwater in arid regions.

1. Introduction

One of the biggest challenges humankind is currently facing is the access to safe drinking water and food supply. This challenge is amplified by the growth in population, and by the consequences of climate change. In particular, low to middle income countries (LMICs) in arid

* Corresponding author at: School of Chemistry, University of Nottingham, University Park, Nottingham, NG7 2RD, United Kingdom.
E-mail address: veerle.vandeginste@nottingham.ac.uk (V. Vandeginste).

https://doi.org/10.1016/j.jhazmat.2020.122150
Received 19 September 2019; Received in revised form 14 December 2019; Accepted 20 January 2020
Available online 20 January 2020

regions are at great risk (Sivakumar et al., 2005). Hence, there is an urgent need to maximize efficient treatment of contaminated waters by using cost effective methods and materials to generate water that is fit for reuse (Asere et al., 2019; Alexander et al., 2019; Han et al., 2019). In many arid regions in LMICs, the mining industry has been or still is active (Fayiga et al., 2018). These mining industrial activities release heavy metals in the environment, which lead to acid mine drainage (with fluids of pH 2–6), and metal contamination of both soil and groundwater (Naz et al., 2016; Pfeiffer et al., 2015; Veado et al., 2006). A study of the Golden Triangle Economic Zone, located in the Eastern Desert stretching between the cities of Qena, Safaga and Qusir in Egypt, has indicated in particular contamination by Mn and Cr (Abdalla and Khalifa, 2013). This study area is known for its mining activities, for example, for gold [Au], wolframite [$(Fe,Mn)WO_4$], talc [$Mg_3Si_4O_{10}(OH)_2$] and phosphate from apatite [$Ca_5(PO_4)_3(OH,F,Cl)$], and the government is investing more resources into this area to stimulate further development in economic growth of this area across three main sectors, namely agriculture, mining and tourism. Several groundwater samples in the study area have a pH of about 7–8 (Embaby et al., 2016), but locally, the sulphides in mine waste from, for example, the Abu Marawat and El-Sid gold deposits, can lead to fluids with pH down to 2 (Zoheir and Akawy, 2010; Zoheir and Moritz, 2014; Gonzalez et al., 2011), and also granite derived sediments in the area are reported to have caused waters with acidic pH of 4.5 (Harraz et al., 2012). Furthermore, the impact of climate change may amplify the effect of acid mine drainage due to more extreme weather events with heavy rainfall and higher temperature, causing the disruption of dams, affecting vegetation cover, and accelerating the chemical reactions involved with sulphide oxidation and metalloid desorption in acid mine drainage (Anawar, 2013). The Golden Triangle Area has very limited surface water, and the industrial and agricultural development in this area relies on groundwater, which is also the source for drinking water (Amer et al., 2012). Hence, this area will need a viable development of sustainable water resources and water management. Moreover, cost effective water treatment is an integral aspect that will need to be incorporated in the development of this area. Mining development and the interrelated need for water management and treatment for reuse is relevant and critical in many arid and semi-arid regions.

Here, we consider the use of natural apatite [$Ca_5(PO_4)_3(OH,F,Cl)$], a mineral extensively available in Egypt (El Maghraby, 2012), that is also abundant in other countries worldwide (such as Morocco), for remediation of groundwater. Natural apatite is the most common phosphate mineral found on Earth. Apatite is a versatile mineral (Hughes, 2015) because of its structure with cation and anion sites that can incorporate more than half of the long-lived elements in the periodic table, leading to the apatite supergroup with over 40 minerals (Hughes and Rakovan, 2015). This characteristic has led to the wide applicability of the mineral, as tracker of metasomatic fluids (Harlov, 2015), as geochronologic and thermochronologic tool (Chew and Spikings, 2015), it can reveal information on diverse magmatic systems (Webster and Piccoli, 2015) and the Solar System (McCubbin and Jones, 2015), and it can be used in technological applications in biomedicine, material science and environmental remediation (Rakovan and Pasteris, 2015). Moreover, in the context of water treatment, apatite is a favourable material because toxic metals can be easily immobilized by the formation of highly insoluble metal phosphate materials which are stable over a wide range of pH values found in the natural environment (Ruby et al., 1994; Smiciklas et al., 2008). Previous studies have tested the removal efficiency of some heavy metals from contaminated fluids by the use of synthetic apatite (Xu et al., 1994; Oliva et al., 2010; Peld et al., 2004; Dominguez et al., 2008; Viipsi et al., 2013; Wang et al., 2019; Fedoroff et al., 1999; Xu and Schwartz, 1994), natural apatite mineral (Chen et al., 1997a, b; Cui et al., 2016; Shin and Kim, 2016; Li et al., 2016) and phosphate rock (Ma et al., 1995; Mouflih et al., 2005), and bone derived material (Piccirillo et al., 2017; Sljivic-Ivanovic et al., 2015; Al-Asheh et al., 1999).

The mechanism of heavy metal removal by apatite has been the focus of debate (Xu et al., 1994; Xu and Schwartz, 1994; Ma et al., 1993; Valsami-Jones et al., 1998; Oliva et al., 2011), and some relatively recent studies employed electron microscopy techniques to investigate what happens at the apatite surface at the nanoscale upon exposure to Pb-contaminated fluids (Kamiishi and Utsunomiya, 2013). The mechanisms of sorption and dissolution-precipitation are the most common interpretations for heavy metal removal by apatite. The wide range and variety of findings in studies suggest that the mechanism may vary depending on the fluid pH, the type of metal, temperature, metal concentration in the solution, and the specific apatite material used. Metal sorption is mainly facilitated by a high specific surface area of the apatite material (Peld et al., 2004). High reversibility of metal sorption is a characteristic that is favourable for the purpose of regeneration of the sorbent material. However, low reversibility of a material is useful as soil additive and as material for permeable reactive barriers in the treatment and passive remediation of contaminated soils, which may see fluids of a variable pH range (Oliva et al., 2010; Peld et al., 2004).

Many of the previous studies on heavy metal removal by apatite have focused on the removal efficiency of divalent Pb, Cd, and Zn, whereas other metals are less commonly studied. Cation substitution of calcium by some other divalent metals in the apatite structure has been described. However, substitution by a trivalent cation has not been so well documented. Moreover, the experiments in previous studies generally contained metals in solution based on preparation with metal nitrate or chloride salts. However, arid and semi-arid regions commonly have elevated sulfate content, which has also been reported in the Golden Triangle Area. A higher sulfate content is a consequence of soils not being fully leached in arid and semi-arid regions (in contrast to humid regions), with the accumulation of sulfates near the surface as a result. The lower amount of rainfall and the greater amount of soil sulfate leads to a relatively high sulfate content in groundwater in arid and semi-arid regions. Groundwater in these regions generally contains sulfate as its predominant anion. Furthermore, previous studies were mainly conducted at a temperature of around 20–25 °C, which do not reflect the temperatures observed in the arid environment, at times reaching to > 45 °C. Here, the aim of our study is to investigate the removal of divalent Mn and trivalent Cr by natural apatite in arid regions by experimental simulation and kinetic tests as a function of fluid pH. The metals Mn and Cr were selected for these experiments based on the significant concentrations found in waters sampled in the Golden Triangle Area based on previous (Abdalla and Khalifa, 2013) and ongoing research. Our experiments are conducted at a temperature of 35 °C, and the metal solutions (with 100 mg L^{-1} metal) are prepared using Mn and Cr sulfate salts. The behaviour of natural apatite and heavy metal removal is tested in a series of solutions with different acidic to neutral pH (1.5–7); the acidic fluids are obtained by addition of dilute sulfuric acid to match the sulfate matrix.

2. Methodology

2.1. Starting material

The starting material is a natural apatite mineral sourced from Madagascar. Natural apatite was selected for this study, because it underpins more sustainable and economical ways for water treatment in arid LMICs, rather than synthetic hydroxyapatite [$Ca_5(PO_4)_3OH$]. The sample has a light blue to turquoise colour. It contains a few light brownish stained fractures, which were not used in the experiments by hand picking the unaltered parts of the mineral upon coarse crushing. The mineral sample was then ground to a fine powder (< 125 µm, confirmed by dry sieving) using an agate mortar and pestle, and cleaned with deionized water to remove microparticles, filtered and dried in a drying oven at 50 °C for three days. This apatite powder was subsequently used in the batch reactor experiments. The remaining apatite was stored in a closed vial at room temperature.

2.2. Heavy metal removal batch reactor experiments

Two series of batch reactor experiments were carried out, one focused on manganese removal and the other one focused on chromium removal. Both series consisted of a range of fluid pH, which enabled assessing the impact of fluid pH on the apatite dissolution rate, as well as metal removal rate and behaviour. The pH range used in our experiments (1.5–7) covers that found in acid mine drainage fluids. The experiments followed both the same overall procedure. An aliquot of 200 mg of apatite powder was added to 100 mL solution in a batch reactor. The prepared solutions contained 100 mg L^{-1} metal, and were prepared by adding $MnSO_4$ hydrate (Fisher Chemicals) or $Cr_2(SO_4)_3$ hydrate (STREM Chemicals) to milliQ water. The concentrations of Mn and Cr in solution are taken the same (100 mg L^{-1}) in both experimental series for comparison purposes of the kinetics of both systems. The concentrations of these metals in bedrock, surface and lake sediments are well beyond 100 mg L^{-1} (about 500 mg L^{-1} for Mn (Mansour and Sidky, 2003)), meaning leaching of the sediments with predicted increased mining activities can exceed the values of 1 mg L^{-1} reported for groundwater in the Golden Triangle Area away from mining activity. Moreover, the selected concentration of 100 mg L^{-1} in our experiments is similar to that used in previous experiments with apatite using 5 – 500 mg L^{-1} Pb (Ma et al., 1993), 150 mg L^{-1} Pb, Cd, Zn (Chen et al., 1997a), 100 – 450 mg L^{-1} Pb, Cd (Valsami-Jones et al., 1998), 30 – 75 mg L^{-1} Zn, Pb, Mn, Fe (Oliva et al., 2010). The pH varying from 1 to 7 in the different experiments was obtained by addition of trace metal grade H_2SO_4 (VWR Chemicals) or NaOH (VWR Chemicals) to the solution. The addition of amounts of concentrated H_2SO_4 were calculated to obtain fluids of pH 1–6; however, the pH in Cr sulfate solutions resulted in more acidic pH due to the formation of Cr complexes. Sulfuric acid and sulfate salts were selected in this study for our experiments because groundwater in arid regions can contain more sulfate than chloride, e.g. in the Golden Triangle in Egypt (Abdalla and Khalifa, 2013), and metal removal in sulfate fluids has not received much research so far. The reactor was put on a Stuart hotplate stirrer, which was maintained at 35 °C ± 0.5 °C, as controlled by a Stuart temperature probe immersed in the solution. The solution was continuously stirred using a magnetic stirrer bar. Fluid samples of 1 mL were collected at selected time intervals throughout the duration of the experiments over 4 weeks, and pH was measured at the same times using a Fisher Scientific accumet benchtop pH meter. The collected fluid was filtered using a 0.22 µm PES filter, and subsequently 800 µL of the filtered solution was diluted 10 times in a 2 % HNO_3 matrix in preparation for geochemical element analysis to determine the concentration of Ca, P and Mn or Cr. A quarter of the experiments was duplicated and duplicate results were within 5 % error, or within 3 mg L^{-1}.

To test the competitive effect between chromium and manganese removal using apatite, an additional experiment was conducted following a similar procedure as described above. In this experiment, 200 mg apatite powder was added to 100 mL solution which contains both 100 mg L^{-1} chromium and 100 mg L^{-1} manganese. The starting pH of this solution was 3.7, and the experiment was run over 4 weeks. At several time intervals, the pH was measured and fluid samples were collected for further analysis of the elemental composition, as described above.

2.3. Far from equilibrium mineral dissolution rate experiments

In addition to the heavy metal removal experiments, two series of experiments were conducted to determine the natural apatite far from equilibrium dissolution rate. The same procedure was applied as for the Mn and Cr sulfate experiments described above. However, here the batch reactor experiments were only run for a total of eight hours with fluid sampling and pH measurements every hour. A quarter of the experiments was duplicated and results were within 5 % error.

2.4. Analytical methods

The composition of the starting material, and reaction products of the batch reactor experiments were analysed by a range of methods. Powder X-ray diffraction (PXRD) analyses were conducted on an PANalytical X'Pert Pro X-ray diffractometer which uses CuKα radiation at a tube voltage of 40 kV and current of 40 mA. The apatite starting material as well as the reaction products were scanned over a sampling range of 5–70 º2θ, with a step size of 0.0066° and a scan speed of 0.023°2θ per second. Data were analysed using the DIFFRAC.EVA software for phase identification by comparison with reference spectra within the PDF4 database (from the International Centre for Diffraction Data).

^{1}H, ^{19}F and ^{31}P nuclear magnetic resonance (NMR) spectra of the (solid) starting material were obtained at magic angle spinning (MAS) rates of up to 50 kHz at 14.1 T. In addition, using high field, ^{43}Ca MAS spectra were collected at the UK 850 MHz solid-state NMR Facility. The latter spectrum was acquired at a Larmor frequency of 57.22 MHz and a MAS rate of 4 kHz on a 7 mm MAS probe. The signal was enhanced using six double frequency sweeps (DFS) per acquisition, each lasting 2 ms, followed by selective excitation of the central transition. There were 71,884 scans with a relaxation delay of 1 s, resulting in a 20 h experiment. The spectral width was 100 kHz and the acquisition time was 10.2 ms. The chemical shift scale was referenced by comparison with the Ca(I) peak position found previously for apatite Laurencin et al. (2008) corrected for the field strength of 20.0 T employed here. The apatite starting material as well as the reaction products were analysed by Fourier Transform Infrared (FTIR) spectrometry (on the solid materia) using a Bruker Alpha FTIR spectrometer to record transmittance for the wavenumber range of 400–4000 cm^{-1} and the data were analysed using OPUS software.

Electron Probe Micro Analysis (EPMA) was carried out on a polished thick section using a JEOL JXA-8200 microprobe instrument with operating voltage of 15 kV, a current of 20 nA, and a defocused 10 µm beam. A defocused beam was used to mitigate F mobility (Stormer et al., 1993). The Brunauer-Emmett-Teller (BET) surface area was determined (with triplicate analysis) using a Micromeritics 3Flex instrument with nitrogen gas for surface characterization of the starting material (apatite) powder used in the batch reactor experiments. Prior to the measurement, the sample powder was degassed overnight at a temperature of 100 °C.

Inductively coupled plasma – optical emission spectrometry (ICP-OES) analyses were carried out on the fluids from the batch reactor experiments using a Perkin Elmer spectrometer Optima 2000 DV. A standard solution containing 28 elements at 100 mg L^{-1} (Fisher Chemicals) as well as a separate standard solution for phosphorus at 1000 mg L^{-1} were used to make a calibration series of 0.1, 1, 3, 5, 7 and 10 mg L^{-1} solutions with 2 % HNO_3 matrix. The concentrations of Ca, P, Mn and Cr were measured in the solutions sampled from the batch reactor experiments.

2.5. Calculation of dissolution rate from batch reactor experiments

The natural apatite far from equilibrium dissolution rate was determined for a series of different pH in both the Mn sulfate and Cr sulfate far from equilibrium mineral dissolution rate experiments as described in section 2.3. The data from these far from equilibrium mineral dissolution rate experiments were also compared with dissolution rates calculated from the first four measurements in the heavy metal removal batch reactor experiments as described in section 2.2 (within the first 26 h of the experiments), which showed dissolution rate results consistent within 1×10^{-9} mol m^{-2} s^{-1} error. The experiments with the lowest pH (1.3) were not used for the calculation of the apatite dissolution rate, since the entire apatite sample dissolved within the first 2 – 3 hours in the experiment, and hence, no reliable dissolution rates could be derived from those experiments. Thus, the

apatite dissolution rate data are presented for the experiments with pH of 1.8 to around 6. In the experiments with pH of 1.8–1.9, data of only the first six hours were used, whereas the experiments with pH of around 3–6, the data from the full eight hour range was used for the dissolution rate calculation. The pH average and standard deviation of the data used in each dissolution rate determination is calculated and presented. The pH standard deviation is less than 0.1 (except in two cases where it is less than 0.3).

The apatite dissolution rate in batch reactor experiments is obtained by the change in concentration of chemical elements (constituents of the apatite mineral) over time, and taking account of the amount of fluid in the reactor, the total apatite surface area, and the stoichiometry of the element in comparison to the apatite mineral. The total apatite surface area is determined by the BET surface area (in $m^2\,g^{-1}$) multiplied by the amount of apatite material in the reactor (in g). We have taken the apatite mass decrease (by ongoing dissolution) over time into account in our calculation, as well as the change in fluid volume in the reactor by sample collection (of 1 mL decrease with each fluid sampling). Moreover, due to the nature of batch reactor experiments, the fluid chemistry changes over time due to the on-going mineral dissolution with release of calcium and phosphate in solution, and increase in pH, therefore, data used for the dissolution rate calculation are taken over a time series at the beginning of the experiment where there is a linear regression of concentration and time, following the equation below. Given the presence of Cr or Mn in the solutions in our experiments, which may be removed from solution by incorporation in the apatite crystal structure by the process of dissolution-precipitation, as documented for example for Pb removal (Oliva et al., 2010; Ma et al., 1993), the Ca concentration rather than P is used for apatite dissolution rate calculation. Hence, the stoichiometric factor to be used for Ca is 5, since 5 mol of Ca are released in the solution for 1 mol of apatite dissolution, based on the chemical formula for calcium fluorapatite, $Ca_5(PO_4)_3F$. The apatite dissolution rate is thus calculated using the following equation:

$$r = \frac{1}{5}\frac{d[Ca]}{dt}\frac{V_f}{A}$$

where r refers to the apatite dissolution rate (in mol $m^{-2}\,s^{-1}$), $[Ca]$ to the Ca concentration in the solution (in mol L^{-1}), t to time (in seconds), V_f to fluid volume (in L), and A to the total surface area of the apatite sample (m^2).

3. Results

3.1. Characterization of natural apatite starting material

The mineralogical structure of the natural apatite sample was characterized by XRD, and the diffractogram (Fig. 1) indicates a fluorapatite [$Ca_5(PO_4)_3F$] crystal structure (Young et al., 1966) rather than hydroxyapatite [$Ca_5(PO_4)_3OH$] or chlorapatite [$Ca_5(PO_4)_3Cl$] (Hughes et al., 1989, 1990). The main diffraction peak (31.89° with corresponding d-value of 2.804 Å) is slightly shifted towards lower angle for hydroxyapatite in comparison with fluorapatite (Fig. 1). Moreover, the fluorapatite structure is confirmed by the NMR spectrum (Fig. 2). This interpretation is based on previous NMR research on fluorohydroxyapatites [$Ca_5(PO_4)_3(F,OH)$] which suggested that the relative intensities for Ca(I) and Ca(II) peaks vary as a function of F^- content (Chen et al., 2015). For hydroxyapatite, there are two peaks at 9.6 ppm and —5.6 ppm relative to saturated $CaCl_2$(aq) with an intensity ratio of 1.5, as suggested by the hydroxyapatite crystal structure. As the F^- content increases, the Ca(II) peak is deshielded and broadens, possibly because of the migration of F^- ions through the channels (Jay et al., 2012), eventually becoming lost in the noise, whereas the Ca(I) peak remains unchanged.

The main vibrational bonds in the apatite samples were characterized by the FTIR transmittance spectrum (Fig. 3), further identifying the

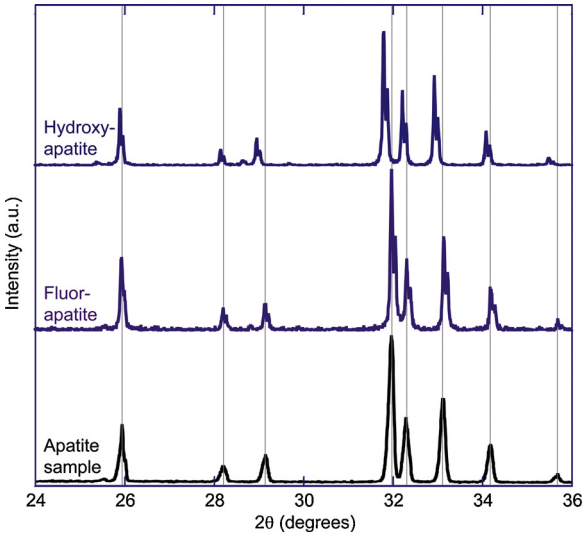

Fig. 1. XRD diffractogram (selected 24–36 °2θ range) of the apatite starting material and comparison with the fluorapatite and hydroxyapatite reference diffractograms.

starting material as fluorapatite. The very strong absorption bands at 568 and 599 cm^{-1} are assigned to components of the triply degenerate ν_4 OPO bending mode (Fowler, 1974). The very strong absorption band with main peak at 1026 and on its shoulder at 1092 cm^{-1} correspond both to triply degenerate ν_3 antisymmetric PO stretching mode (Domínguez et al., 2008; Antonakos et al., 2007). Additional absorption bands on the shoulder of the 1026 main peak towards lower wavenumbers include the absorption at 962 and 864 cm^{-1} which is assigned to ν_1 PO stretching mode, and to ν_2 CO_3 (B-type substitution) modes, respectively. The weak absorption band at 923 cm^{-1} may be attributed to the ν_3 mode of silicate anions in the apatite network (Domínguez et al., 2008). The weak absorption peaks at 1424 and 1453 cm^{-1} correspond to the ν_3 CO_3 francolite bands (Antonakos et al., 2007), these are stretching vibrations of carbonate ions which have replaced phosphate groups in the crystal (Fleet and Liu, 2003, 2004). No clear absorption is observed at 3570 cm^{-1}, which corresponds to the OH stretching mode (Fowler, 1974), which would be expected for hydroxyapatite. The FTIR results thus indicate that the natural sample is fluorapatite with minor carbonate and silicate in its structure. The chemical composition of the natural apatite sample is measured by EPMA analysis, presented in Table 1, and indicates a molar Ca/P ratio of 1.77. The surface area of the apatite powder used in the batch reactor experiments was measured by nitrogen BET analysis, and is 0.43 ± 0.03 $m^2\,g^{-1}$.

3.2. Interaction of natural fluorapatite with manganese sulfate solutions

Six experiments were conducted to investigate the interaction of natural fluorapatite with manganese sulfate solutions of different initial pH (1.6, 2.3, 2.8, 4.1, 4.9, 6.6). The results of these batch reactor experiments show that the pH increases with time (except for the lowest pH 1.6 experiment) with a faster increase (of up to 0.03 per hour) at the start of the experiments and approaching equilibrium (with pH measurements within error of each other) near the end of the experiments (Fig. 4). The Ca concentration in the batch reactor experiments also increases with time, with a fast increase at the start and then a more gentle increase (Fig. 4), when the system gets closer to equilibrium, as reflected by the respective pH trend. The Ca concentration in the fluids increases more in the experiments with lower pH. Only in the experiment with pH of 1.6 does the Ca concentration reach that expected for complete dissolution of the apatite (200 mg) introduced in the solution (100 mL) in the reactor. In all other experiments, only part of the Ca

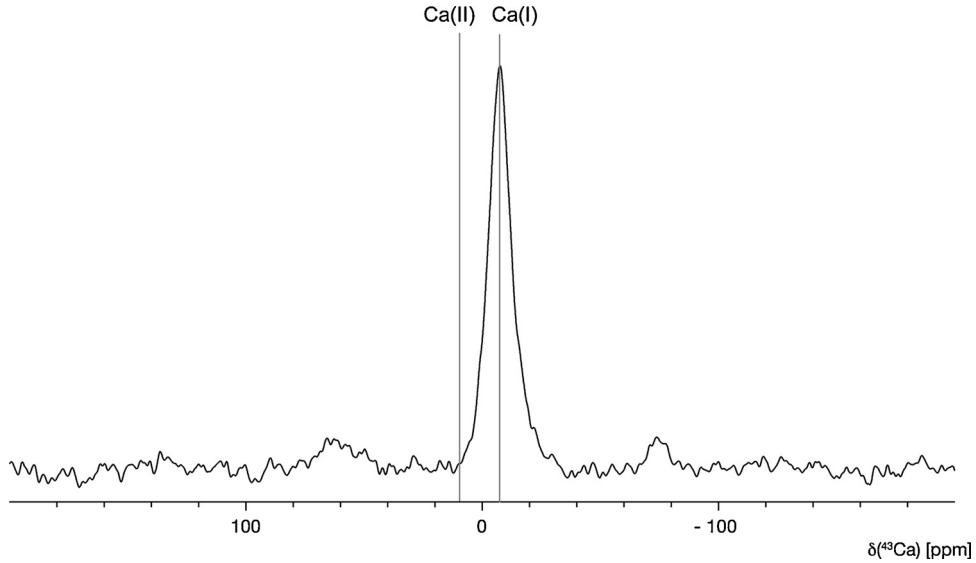

Fig. 2. ^{43}Ca DFS enhanced MAS NMR spectrum of apatite starting material. The Ca(I) and Ca(II) chemical shifts are indicated based on previous work on hydroxyapatite that shows the impact of fluorine in the apatite structure on dramatically decreasing the relative intensity of the Ca(II) to Ca(I) peaks (Chen et al., 2015).

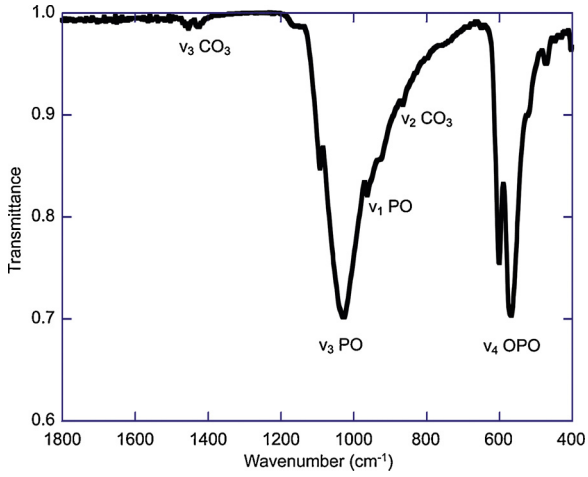

Fig. 3. FTIR spectrum of the natural fluorapatite starting material with the main bands labelled.

Table 1
Chemical composition (weight%) of the apatite sample based on EPMA analysis. The average and standard deviation is presented based on a total of 20 analyses.

Element	Average	Standard deviation
Ca	39.340	0.330
P	17.216	0.241
F	3.724	0.505
Cl	0.257	0.048
Mn	0.035	0.009
Fe	0.006	0.007
K	0.002	0.002
Mg	0.006	0.002

from the apatite sample is released into solution within the duration of the experiments, namely 42 %, 12 %, 6.9 %, 6.6 %, and 2.3 % of the original starting material for the experiments with starting pH of 2.3, 2.8, 4.1, 4.9, and 6.6, respectively, for 548 h reaction time.

The results of the Mn concentration measured in the fluids from the batch reactor experiments indicate no significant decrease (with values within 5 % experimental error) in batch reactor experiments with initial pH of 1.6 and 2.3 (Fig. 4). In contrast, the experiments with initial pH of 2.8, 4.1, 4.9 and 6.6 show removal of Mn from solution (Fig. 4), with more removal achieved at higher pH over the course of the experiments (although Mn removal is very similar for experiments with initial pH of 4.1 and 4.9). A decrease in Mn concentration in the fluids is observed only after a delay from the start of the experiment with initial pH of 2.8. The concentration of P in this experiment shows an increase that linearly correlates with Ca increase (with molar Ca/P = 1.8) for the first six data points (within the first 100 h of the experiment, when the solution pH is below 5), after which Ca continues to increase in the solution but P remains stable, resulting in an increasing molar Ca/P ratio (Fig. 5). For the experiment with initial pH of 6.6, a minor amount of NaOH was added to obtain this pH, which resulted in immediate formation of pale brown staining of the solution. The concentration of Mn is immediately much lower than in any other experiment, but then still further decreases over the duration of the experiment. Similar to the low Ca concentration in the fluids in this experiment, the P concentration is even lower, remaining below 0.07 mmol L^{-1}.

The solid reaction products from the batch reactor experiments were characterized by XRD, FTIR (Fig. 6), SEM-EDS (Fig. 7) and EPMA to assess potential changes in the mineral structure and chemistry. For experiment with initial pH of 1.6, no apatite remains in the reaction product. Instead, the minor amount of reaction product in the reactor at the end of the experiment was identified as gypsum [$CaSO_4.2H_2O$] by XRD with a main diffraction peak at 11.7°2θ, corresponding to d-value of 7.6 (Wooster, 1936). This result was confirmed by FTIR data, with a doublet in the spectrum at 593 and 665 cm^{-1} (Fig. 6), assigned to the ν_4 SO_4 asymmetric bending vibration (Salisbury et al., 1991; Ross, 1974). Sharp doublet bands at 1619 and 1683 cm^{-1} correspond to H_2O bending vibrations, and the main band at 3396 cm^{-1} and minor band at 3494 cm^{-1} to H_2O stretching vibrations. The band at 1102 cm^{-1} is attributed to absorbance from ν_1 and ν_3 SO_4 vibrations (Bishop et al., 2014).

In the other experiments (pH 2–7), no differences were detected in the reaction product XRD diffractograms in comparison to the apatite starting material. Similarly, the bands observed on FTIR spectra for the reaction products have very similar wavenumbers to those in the apatite starting material (Fig. 6). However, the transmittance of the main bands assigned to vibrations of phosphate and carbonate groups are lower, and thus the bands are even more pronounced. The SEM images show that some grains in the apatite starting material have a few apatite microparticles attached which remained after cleaning of the starting

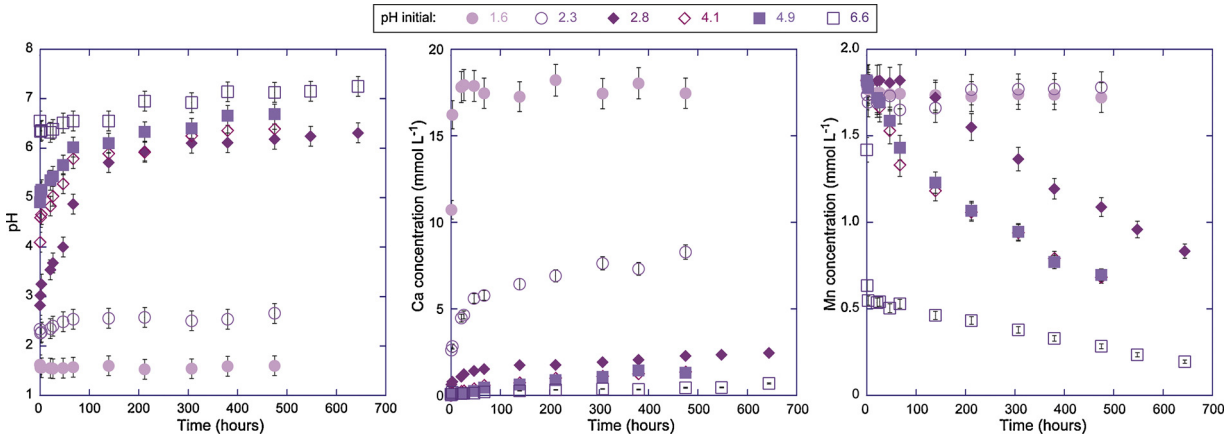

Fig. 4. Fluorapatite – manganese sulfate solution batch reactor fluid chemical data as a function of time, with pH, Ca concentration and Mn concentration for the series of experiments with different initial pH.

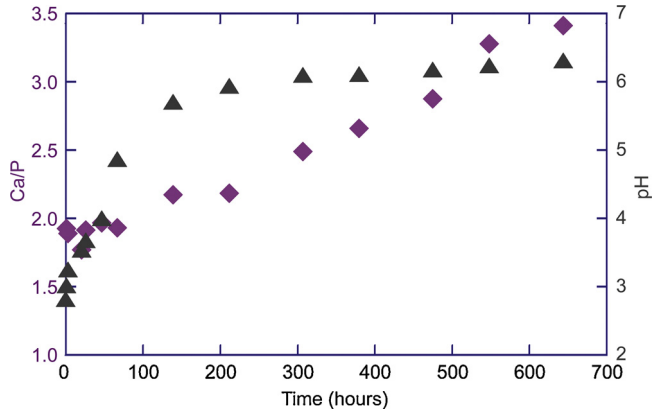

Fig. 5. Fluid chemical data plot showing molar Ca/P ratio and pH against time in the fluorapatite – manganese sulfate solution batch reactor experiment with initial pH of 2.8. The plot presents a constant Ca/P ratio for data collected within the first 100 h with solution at pH less than 5, followed by Ca/P increase in solution when pH has increased beyond 5.

material with deionized water before use in the experiments. The images of the reacted samples demonstrate the development of apatite dissolution zones and growth of small Mn-containing phosphate crystals on the apatite grains, and thus show a less smooth surface in comparison to the apatite before reaction which does not display dissolution zones (Fig. 7 A–B). Further EPMA analysis on the reaction products indicate the presence of apatite crystals, with 39.5 ± 0.1 wt% Ca and 16.8 ± 1.2 wt% P, and very fine Mn-containing crystals, with 27.5 ± 1.8 wt% Mn, 11.8 ± 1.1 wt% P and 2.3 ± 1.0 wt% Ca. Despite the clear pale brown staining of the solution with initial pH of 6.6, no clear difference in mineralogy was detected by XRD or FTIR.

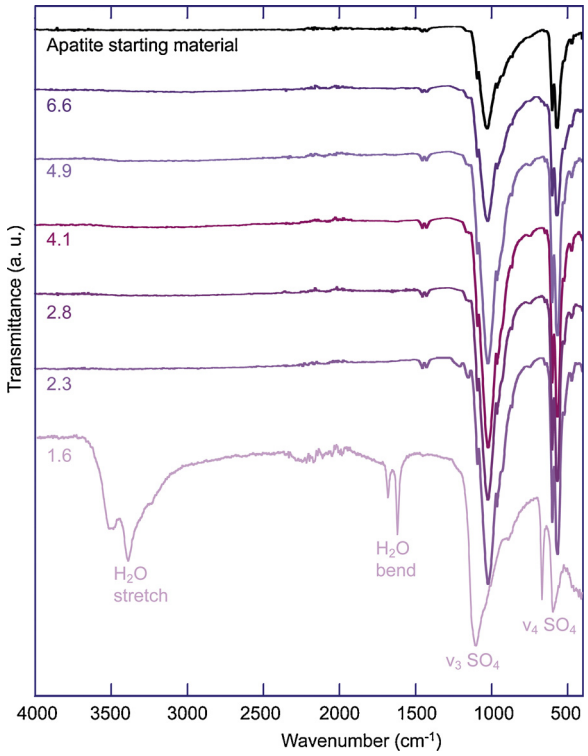

Fig. 6. FTIR spectra of the reaction products from the natural fluorapatite – Mn sulfate solution batch reactor experiments, with the FTIR spectrum of the natural fluorapatite starting material for comparison. The spectra are indicated with the value of the experiment fluid initial pH, and the main bands are labelled for the pH 1.6 spectrum, whereas the main bands in apatite can be compared with those labelled in Fig. 3.

3.3. Interaction of natural fluorapatite with chromium sulfate solutions

A total of seven experiments were run to study the interaction of natural fluorapatite with chromium sulfate solutions of different initial pH (1.5, 2.0, 2.8, 3.3, 3.4, 4.6, 7.0). As in the manganese experiments, the pH of the fluids increases with time (Fig. 8). The Ca concentration in fluids in the batch reactor experiments increases with time, and shows faster increase at the start of the experiments in comparison to later in the experiments (Fig. 8). Only in the experiment with initial pH of 1.5, a decrease in Ca concentration in the fluid is recorded after a fast increase within the first 20 h of the experiment. The highest concentration recorded corresponds to the dissolution of all apatite (200 mg) introduced in the reactor. There is a decrease of only about 0.39 mmol L^{-1} Cr in the fluids in experiments with initial pH of 1.5 and 2.0 (from the initial 1.92 mmol L^{-1} Cr in the solution). However, the results from the other, higher initial pH, experiments, show a major decrease of Cr concentration until 0 to 0.42 mmol L^{-1} remaining in solution depending on the pH of the experiment (0 for pH 4.6 and 7.0, and 0.42 mmol L^{-1} for pH of 2.8), with faster Cr decrease in fluids with higher pH (Fig. 8). Removal of Cr from the fluid starts immediately in the experiments with initial pH of 4.6 and 7.0, whereas the Cr decrease only starts after a delay in the lower pH experiments. In the experiment with starting pH of 3.3, the molar Ca/P ratio remains constant for the first 50 h, and then increases significantly (Fig. 9). The measured P concentration in the experiment with pH 4.6 indicates that this concentration in the solution

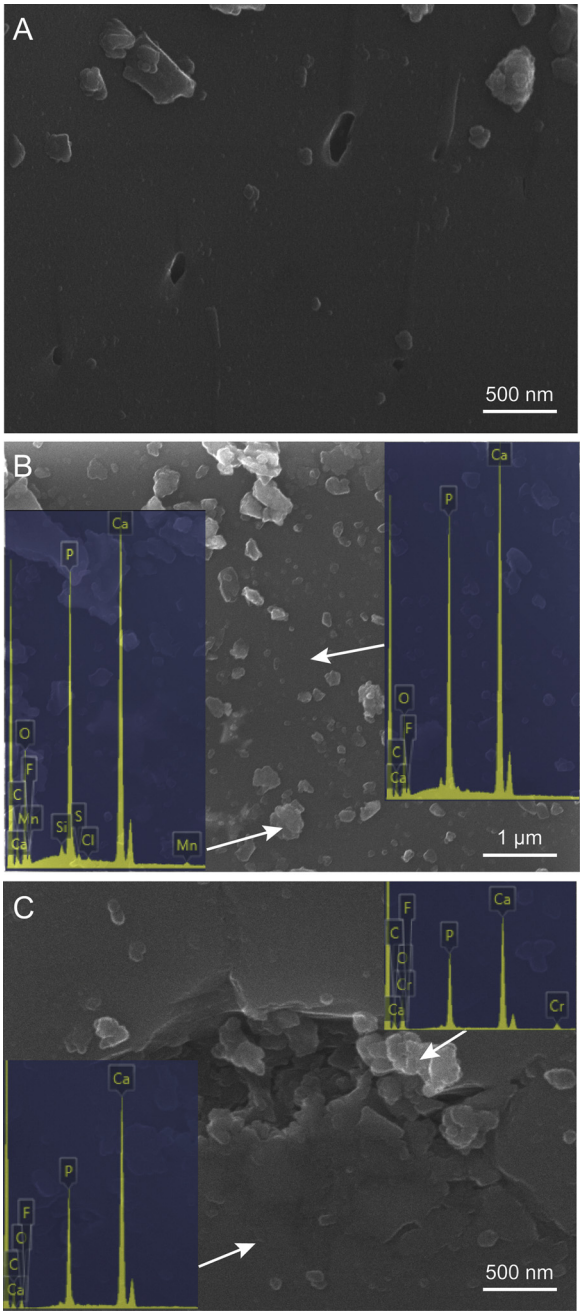

Fig. 7. SEM images of apatite starting material (A), apatite after 4 weeks reaction with Mn sulfate solution with starting pH of 2.8 (B), and apatite after 4 weeks reaction with Cr sulfate solution with starting pH of 4.6 (C). Qualitative EDX spectra are added showing the additional presence of Mn (B) and Cr (C) in small particles in comparison to the flat apatite surface.

remains low, not exceeding 0.2 mmol L^{-1}, and in the experiment with initial pH of 7.0, the P concentration does not exceed 0.03 mmol L^{-1}.

The reaction products from these experiments investigating the interaction of natural fluorapatite with chromium sulfate solutions were characterized by XRD, FTIR (Fig. 10), and EPMA. Similar to the pH 1.6 experiment with manganese sulfate solutions, also in the chromium sulfate solution series the experiment with initial pH of 1.5 all apatite dissolved and the recovered reaction product was identified as gypsum [$CaSO_4.2H_2O$] based on XRD and FTIR analysis (Fig. 10). In the experiments with starting pH of 2–7, the main reaction products were identified as fluorapatite based on XRD. Also the FTIR spectra of the reaction products show the characteristic bands expected for apatite similar to the apatite starting material (Fig. 10). However, in contrast to the reaction products from the manganese sulfate experiments, a very broad minor band is also detected in the region around 3250 cm^{-1} which may be attributed to H_2O stretching vibrations, in particular in the reaction products from experiments with initial pH of 2.8, 3.3 and 3.4. The SEM-EDS data show that the small apatite crystals at the surface have a higher Cr content than the flat surface of the apatite crystal (Fig. 7C). Further EPMA analysis of the reaction products indicate fluorapatite crystals with 39.5 ± 1.0 wt% Ca and 15.2 ± 0.5 wt% P, and very fine Cr-containing particles, with 6.1 ± 2.5 wt% Cr, 7.6 ± 1.8 wt% P and 10.6 ± 3.1 wt% Ca.

An additional experiment with starting pH of 3.7 to test the competition between chromium and manganese shows that chromium is preferentially removed from solution during the 4 week long experiment (Fig. 11). Similar to the chromium experiments with starting pH below 4, the pH does not increase above 5 within the 4 weeks duration of the experiment, in contrast to the pH increase in the manganese experiments. No significant removal of Mn is detected in these Cr-Mn sulfate experiments.

3.4. Kinetics of natural fluorapatite far from equilibrium dissolution in Mn and Cr sulfate solutions

The rates of natural fluorapatite dissolution in the sulfate solutions of different pH were derived from the calcium concentration data from the experiments. The far from equilibrium conditions are considered here, taking account of the first eight hours of reaction with time (with pH standard deviation < 0.3). The calcium concentration data are not affected by potential calcium sulfate precipitation which only started after about 100 h in the heavy metal removal batch reactor experiments with the lowest initial pH of 1.5, whereas the far from equilibrium apatite dissolution experiments are run for only 8 h with an initial pH of 1.8 or higher. The calcium concentration data show a linear trend with time (Fig. 12), and the fluorapatite dissolution rates are calculated based on normalization for the apatite sample surface area, using the initial BET surface area per gram and taking account of decrease in amount of grams as the dissolution reaction proceeds. The fluorapatite dissolution rate increases with decreasing fluid pH, varying from 1.9×10^{-10} mol m^{-2} s^{-1} for fluid pH of 5.8 to 1.0×10^{-8} mol m^{-2} s^{-1} at fluid pH of 1.9 (Table 2).

4. Discussion

4.1. Kinetics of fluorapatite dissolution rate as a function of pH

The dissolution reaction of fluorapatite in the acidic pH range is the following:

$$Ca_5(PO_4)_3F + 3H^+ \leftrightarrow 5Ca^{2+} + 3HPO_4^{2-} + F^-$$

Fluorapatite dissolution rates were calculated for experiments with initial pH of 1.5–4.9, and compared with fluorapatite dissolution rates from previous studies. The fluorapatite dissolution rates in our study for pH of around 5 and 6 are very similar to the rates presented in studies by Guidry and Mackenzie (2003), Welch, Taunton and Banfield (Welch et al., 2002) and Chairat, Schott, Oelkers, Lartigue and Harouiya (Chairat et al., 2007) (Fig. 13). However, the rates calculated for experiments with pH of 1.8–3.3 are up to 10 times slower. Given that our experiments were conducted at higher temperature (35 °C) in comparison to the other studies (which were carried out at 22 and 25 °C), a faster dissolution rate would have been expected. We interpret the slower rates in our study for those experiments to be caused by the change in fluorapatite saturation state of the fluids in the batch reactors, and potentially by a change in the apatite sample surface area. As apatite dissolves in the solution during the on-going fluorapatite batch reactor experiments, the fluid becomes gradually less

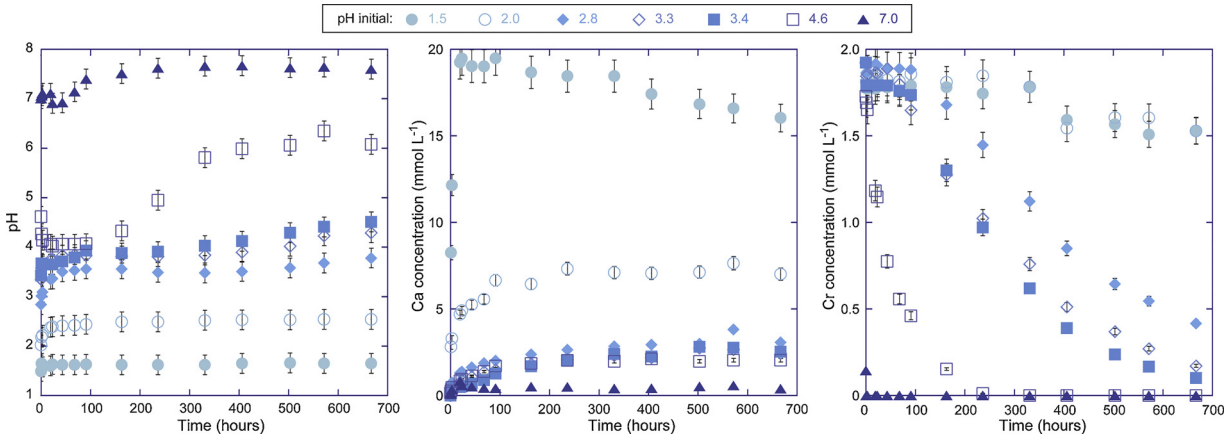

Fig. 8. Fluorapatite – chromium sulfate solution batch reactor fluid chemical data as a function of time, with pH, Ca concentration and Mn concentration for the series of experiments with different initial pH.

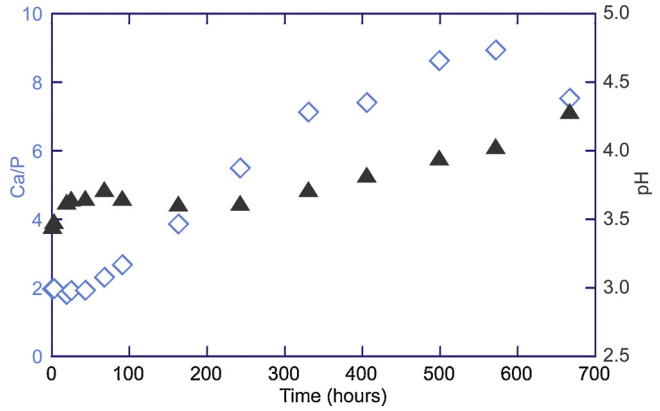

Fig. 9. Fluid chemical data plot showing molar Ca/P ratio and pH against time in the fluorapatite – chromium sulfate solution batch reactor experiment with initial pH of 3.3. The plot presents a constant Ca/P ratio for data collected within the first 50 h, and an increase in Ca/P ratio thereafter.

undersaturated with respect to fluorapatite, which causes a decrease in dissolution rate. Moreover, our calculation takes account of the change in total amount of apatite material during the reaction, but not of the surface area per gram; however, it is possible that highly reactive sites with high surface area react preferentially and quickly within the first hour, and that this leads to an overall decrease in surface area per gram, which could cause the observed lower dissolution rate. The presence of metal sulfate in the solution could potentially impact the fluorapatite dissolution rate as well. Addition of heavy metals such as Cd, Cu, Mn, Pb and Zn in solution have shown to cause a decrease in the dissolution rate of synthetic biogenic hydroxyapatite (Oliva et al., 2012). Such result is a known phenomenon attributed to the formation of metal surface species at the mineral surface which slow down dissolution (Alkattan et al., 1997). However, other studies on synthetic hydroxyapatite do not report significant differences in apatite dissolution rate by addition of Pb in solution (Valsami-Jones et al., 1998), and the apatite dissolution rates measured in our study are only lower than reported values for the low pH experiments, not those with pH of 5–6 (which have the same metal concentrations). Hence, the most likely cause of the measured slower dissolution rates for the low pH experiments in our study may be attributed to the change in saturation state of the fluid and change in mineral surface during the reaction period recorded. Additional potential factors that can affect mineral dissolution include experimental conditions such as stirring rate / agitation, apatite composition (mineral impurities), mineral powder grain size, solid/solution ratio, salinity of the fluid, surface energy and surface area

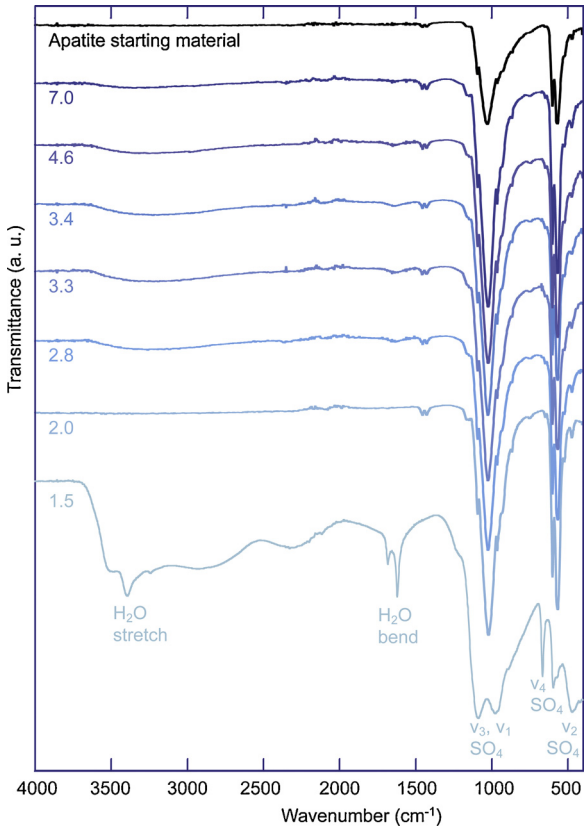

Fig. 10. FTIR spectra of the reaction products from the natural fluorapatite – Cr sulfate solution batch reactor experiments, with the FTIR spectrum of the natural fluorapatite starting material for comparison. The spectra are indicated with the value of the experiment fluid initial pH, and the main bands are labelled for the pH 1.5 spectrum, whereas the main bands in apatite can be compared with those labelled in Fig. 3.

change over time (Fischer et al., 2012; Luttge et al., 2019; Dorozhkin, 2002).

A linear fit of the pH dependence of the fluorapatite dissolution rate at 35 °C for the pH range studied shows a slope of —0.4 for the Mn experiments (R = 0.9788), and about —0.7 for the Cr experiments (R = 0.9987), which is similar to that reported in other studies (Guidry and Mackenzie, 2003; Chairat et al., 2007) (Fig. 11). Hence, the fluorapatite dissolution rate based on the Mn experiments can be expressed as a rate constant of 5.7×10^{-8} mol m^{-2} s^{-1} multiplied by the activity of H^+ to the power (reaction order) of 0.4. This follows the

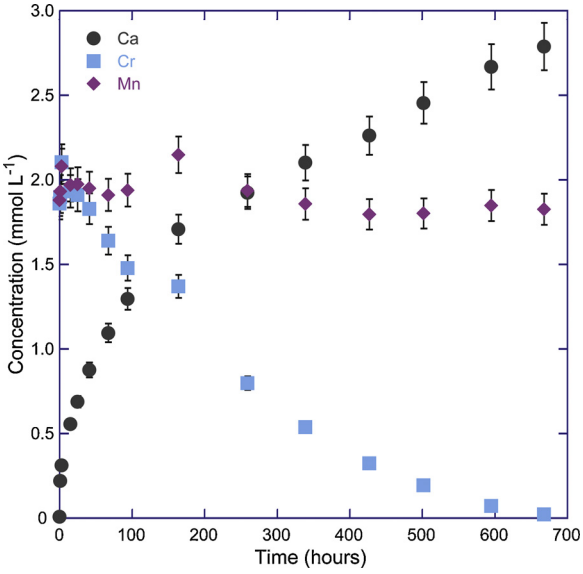

Fig. 11. Fluorapatite – manganese and chromium sulfate solution batch reactor fluid chemical data, presenting Ca, Cr and Mn concentration as a function of time.

equation:

$$r = k\,(a_{H^+})^n$$

where r is the apatite dissolution rate, k is the rate constant, a_{H^+} is the activity of H^+ and n is the reaction order (Harouiya et al., 2007).

In terms of the fluorapatite dissolution mechanism, the fluorapatite structure needs to be considered. Its structure has three cation sites, called T, $M1$ and $M2$ sites. The tetrahedral T site is occupied by phosphate groups. Per unit cell, there are six T sites, four $M1$ sites and six $M2$ sites. The metal $M1$ and $M2$ sites are commonly occupied by Ca in CaO_9 and CaO_6F structures, respectively (Hughes and Rakovan, 2015). The fluorapatite structure contains P-O, Ca-O and Ca-F bonds, and the relative strength of these bonds follows the order of P-O > Ca(II)-O > Ca(I)-O > Ca-F (Chairat et al., 2007), whereby Ca(I) and Ca(II) refer to $M1$ and $M2$ sites, respectively. Consistent with this, previous work has suggested that fluorapatite dissolution is initiated by rapid removal of F from the near surface (Dorozhkin, 2002), and that Ca from

Table 2
Natural calcium fluorapatite dissolution rates calculated based on our experiments with Mn and Cr sulfate solutions. The pH value states the average pH (± stdev) based on the first measurements in the experiment that were taken into account for the apatite dissolution rate calculation.

Starting components	Matrix	pH	Rate (mol m^{-2} s^{-1})
Natural apatite, Mn^{2+}	H_2SO_4	1.88 ± 0.06	1.0×10^{-8}
Natural apatite, Mn^{2+}	H_2SO_4	3.29 ± 0.19	2.3×10^{-9}
Natural apatite, Mn^{2+}	H_2SO_4	5.18 ± 0.30	7.4×10^{-10}
Natural apatite, Mn^{2+}	H_2SO_4	5.79 ± 0.10	1.9×10^{-10}
Natural apatite, Cr^{3+}	H_2SO_4	1.84 ± 0.03	1.2×10^{-8}
Natural apatite, Cr^{3+}	H_2SO_4	2.81 ± 0.07	2.9×10^{-9}
Natural apatite, Cr^{3+}	H_2SO_4	3.25 ± 0.02	1.3×10^{-9}
Natural apatite, Cr^{3+}	H_2SO_4	3.32 ± 0.01	1.2×10^{-9}

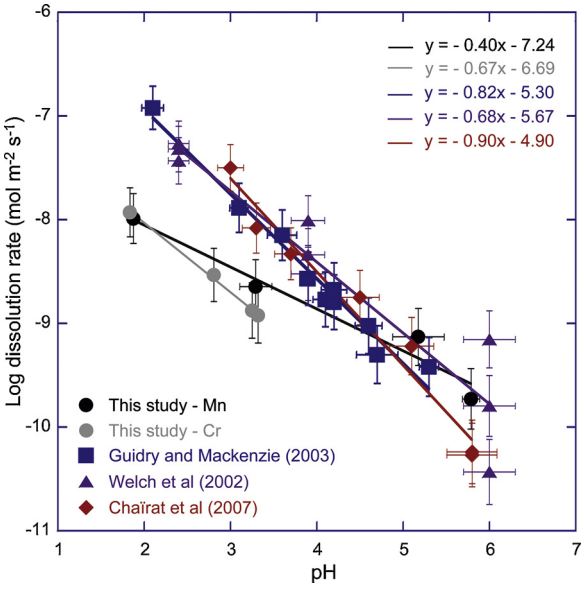

Fig. 13. Logarithm of fluorapatite dissolution rate versus pH for this study at 35 °C and comparison with data from other studies on fluorapatite dissolution at 25 °C (Guidry and Mackenzie, 2003; Chairat et al., 2007) and at 22 °C (Welch et al., 2002).

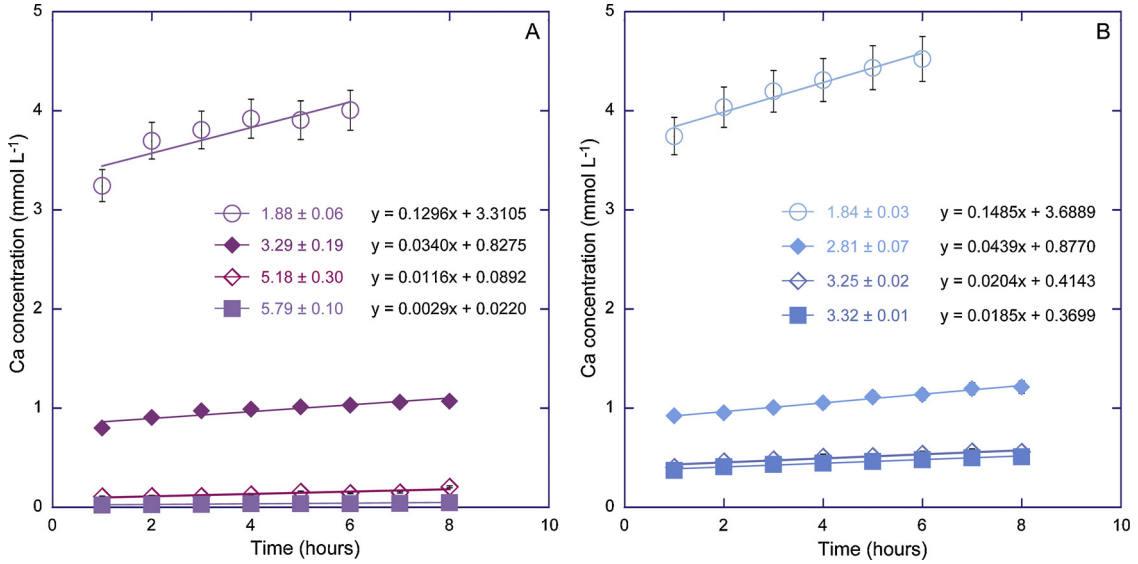

Fig. 12. Far from equilibrium data of Ca concentration against time used for fluorapatite dissolution rate calculation from batch reactor experiments with Mn sulfate solution (A) and Cr sulfate solution (B). The labels represent the fluid pH average for the data points presented.

the *M*1 sites is easier to remove during fluorapatite dissolution than Ca located in the *M*2 sites (Chairat et al., 2007). According to Dorozhkin (2002) and Christoffersen and Christoffersen (1982), H^+ is adsorbed onto fluoride ions and phosphate group oxygen ions. The adsorption of H^+ onto the apatite surface results in a pH increase of the solution in the reactor (Zhu et al., 2009). A pH increase was observed in most experiments in this study, with an increase of up to about 3 pH units in the Mn sulfate experiments, and up to about 1.5 pH units in the Cr sulfate experiments. For fluorapatite dissolution in experiments with pH between 1 and 7, it is suggested that Ca removal is linked with phosphate hydrolysis, the formation of a $CaHPO_4$ layer, and further penetration of protons into the apatite structure with addition of a proton to $CaHPO_4$ forming a protonated precursor complex (Chairat et al., 2007). This is then followed by hydrolysis of the remaining Ca-O bonds (Chairat et al., 2007). Upon desorption of F, Ca and phosphate from the crystal surface, some amount of these from the solution may be adsorbed back onto the apatite surface (Zhu et al., 2009).

4.2. Manganese metal removal as a function of pH

Comparing Mn concentration in solution at specific time intervals from the Mn sulfate experiments at different starting pH indicates that more Mn is removed in solutions with higher pH (Fig. 4). Moreover, the experiments with an initial pH of 1.6 and 2.3 do not show significant Mn removal from solution (considering 5 % experimental error) for the duration of the experiments spanning about three weeks. The Mn removal rate seems similar in the experiments with initial pH of 2.8, 4.1 and 4.9, although a delay in the start of Mn removal is apparent for the pH 2.8 experiment (Fig. 4). The Mn removal rate is very fast initially (62 % removal within the first 3 h) in the experiment with starting pH of 6.6, and then followed by a slower Mn removal rate (a further 25 % removal in the next 640 h) in comparison with the other experiments with initial pH of 2.8, 4.1 and 4.9. This initial fast decrease in Mn concentration in solution is interpreted by fast precipitation of $Mn(OH)_2$, which is partly oxidized to $Mn(|I)Mn(III)_2O_4$, resulting in the immediate formation of pale brown staining, upon addition of NaOH in the solution to obtain a near-neutral solution pH. The formation of $Mn(|I)Mn(III)_2O_4$ (or Mn_3O_4) under those conditions of the experiment have also been confirmed by PHREEQC geochemical modelling, which show oversaturation of Mn hydr(oxides) with $Mn(|I)Mn(III)_2O_4$ being the most oversaturated (Table S1). Upon bonding of Mn with (hydr) oxide from solution, the remaining Mn in the solution could then further be removed by reaction with apatite.

The results of measured Mn lost from solution against Ca gained in the solution show that the mole per mole relation differs with pH of the solution (Fig. 12). There is a clear mole-per-mole trend for the experiments conducted at starting pH of 4.1 and 4.9, suggesting a mole-per-mole exchange of Ca with Mn in the fluorapatite structure, although the data slightly deviate from the 1:1 line with Ca gain in solution being slightly more than Mn loss. The exchange could take place by either solid-state diffusion or a dissolution-precipitation mechanism. Diffusion of Mn into the apatite structure has been described in literature at temperatures of ≥ 900 °C (Gaft et al., 1997), which will not be the driving mechanism observed for this study undertaken at 35 °C resulting in diffusion being extremely slow (Cherniak, 2005). A dissolution-precipitation mechanism is thus most likely to explain the mole-per-mole exchange, which can be driven by a higher solubility of calcium fluorapatite in comparison with a manganese phosphate phase formed in the reaction. Previous research has indicated the formation of switzerite $[Mn_3(PO_4)_2.7H_2O]$ in experiments of biogenic hydroxyapatite (Apatite II™) with Mn solutions (Oliva et al., 2010, 2012). Considering the molar concentrations of Mn lost from solution, Ca gained in solution and changes in P in the solution, we can derive the stoichiometry of the Mn precipitate. The calculated molar Mn/P ratio of the precipitate is 1.44 ± 0.04, assuming a Ca/P ratio of 1.67 for the fluorapatite starting material, or 1.53 ± 0.04, considering a Ca/P ratio of 1.77 according to our EPMA measurements on the starting material. Hence, a molar Mn/P ratio of 1.5 is consistent with the formation of switzerite $[Mn_3(PO_4)_2.7H_2O]$ in our experiments. This also explains the slight deviation from the 1:1 line, since the expected Mn lost to Ca gained ratio is 0.9 based on fluorapatite dissolution and switzerite precipitation and the different molar Ca/P and Mn/P ratios in the respective crystals. Moreover, the EPMA measurements on the Mn-containing phases confirm these results. The most likely Mn-containing phosphate phases include switzerite with 34 wt% Mn and 13 wt% P, and hureaulite $[Mn_5(PO_3OH)_2(PO_4)_2.4H_2O]$ with 38 % Mn and 17 % P. The EPMA results show that our reaction products have 28 % Mn, 12 % P and 2 % Ca, and match most closely the switzerite composition, even though our products may have some impurity of Ca either in the structure taking the place of Mn, or in the EPMA signal by neighbouring apatite.

PHREEQC geochemical modelling of each of our experiments has provided information on chemical species distribution and saturation index of different minerals in the solutions. In terms of chemical species distribution, the predominant Ca species are Ca^{2+} and $CaSO_4^\circ$ with increasing contribution of the former and decreasing of the latter with increase in initial pH of our experiments (Fig. S1A). For Mn(II) species distribution, the predominant species are Mn^{2+} and $MnSO_4^\circ$, with minor presence of $MnH_2PO_4^+$. With increasing initial pH of our experiment, Mn^{2+} becomes relatively more abundant, whereas $MnSO_4^\circ$ becomes less abundant (Fig. S1B). For P(V) species distribution, $H_2PO_4^-$ is the predominant species in experiments with initial pH of 2.3, 2.8 and 4.1. H_3PO_4 is dominant in the experiment with initial pH of 1.6, whereas HPO_4^{2-}, $MnHPO_4$ and $MnPO_4^-$ become more important in experiments with initial pH of 4.9 and 6.6 (Fig. S1C). Saturation index results show that the solution of experiment with initial pH of 1.6 is oversaturated with respect to gypsum and anhydrite, in contrast to the other experiments with higher pH. Switzerite, having added this mineral to the llnl database, is oversaturated in all Mn experiments, with higher oversaturation in experiments with higher initial pH; $MnHPO_4$ shows a similar trend although with lower absolute saturation index values. Manganese (hydr)oxides (Mn_2O_3, Mn_3O_4, MnO(OH), MnO_2) are oversaturated in experiment with initial pH of 4.1, and even more in the experiment with initial pH of 6.6 (Table S1). The saturation index of manganese (hydr)oxides decreases in the following order $Mn_3O_4 > Mn_2O_3 > MnO_2 > MnO(OH)$ in experiment with initial pH of 6.6 (Table S1), confirming the expected presence of Mn_3O_4 in the reaction product.

Although the measured Mn loss and Ca gain in solution in the Mn sulfate experiment with initial pH of 2.8 does not follow the mole-per-mole line on the plot, there is a clear mole-per-mole trend but shifted towards higher Ca gain in solution (> 1.5 mmol L^{-1}) as shown in Fig. 14. These results indicate that only fluorapatite dissolution initially takes place without removal of Mn via precipitation or another mechanism. Such interpretation is confirmed by the increase in Ca and P following a correlation of molar Ca/P of 1.8 (Fig. 5), which is close to that expected based on the stoichiometric fluorapatite of 5/3. The dissolution-only phase was then followed by exchange of 1 mol Ca by 0.9 mol Mn by a mechanism of fluorapatite dissolution and switzerite formation similar to that described above. At this stage, the P concentration no longer increases in the solution; in fact, it seems to even slightly decrease, indicating that switzerite precipitation occurs then at a slightly faster rate than fluorapatite dissolution. This delay relates to the pH conditions of the experiment, as fluorapatite dissolution-only is dominant at low pH near the start, and then associated switzerite formation starts when the solution pH in the experiment has reached a value of around 5. This strong pH control on Mn removal further supports the interpretation of a dissolution-precipitation mechanism. Also at conditions with starting pH of 6.6, exchange of 1 mol Ca by 0.9 mol Mn is identified in the experiments, here this occurs after a shift to higher Mn loss values (Fig. 14), which is interpreted to be caused by the reaction of Mn with hydroxide in solution and fast formation of Mn

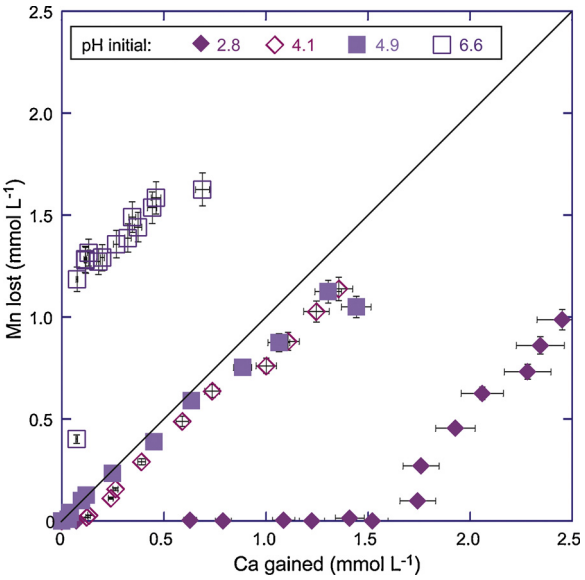

Fig. 14. Correlation of the concentration of Mn lost from solution against the concentration of Ca gained in the solution in the fluorapatite – Mn sulfate solution batch experiments with different initial pH.

$(OH)_2$ and $Mn(|I)Mn(III)_2O_4$ within the first hours of the experiment.

Considering the rate of Mn removal after the initial fast removal for the experiment with initial pH of 6.6 and comparison with the rate in experiments with initial pH of 4–5, it is clear that for the respective experiments a slightly lower pH corresponds to a higher rate of Mn removal from solution (Fig. 4). However, the Mn removal rate could also be influenced by the Mn content in solution, with lower concentration resulting in slower removal rate. The change in Mn concentration in solution over time seems linear, though, in the experiments after initial fast pH change (in the first 100 h). Hence, we consider the change in Mn removal rate to be impacted predominantly by pH in our experiments. This finding further confirms our interpretation on the dissolution-precipitation mechanism; the opposite would be expected in the case of a sorption mechanism. A similar pH influence on the rate of Pb removal in fluorapatite experiments was also reported by Valsami-Jones, Ragnarsdottir, Putnis, Bosbach, Kemp and Cressey (Valsami-Jones et al., 1998).

The results of these batch reactor experiments show that natural fluorapatite is effective in removing Mn from fluids with pH of 4–5. Moreover, for fluids with pH of about 3, apatite dissolves leading to an increase of the pH of the fluids, which can subsequently act to remove Mn from the fluids. Natural fluorapatite can thus be very useful for remediation of Mn rich acid mine drainage fluids. Extrapolating data from batch experiments to flow through porous media to make field scale predictions leads to overestimation due to transport mechanisms and mass transfer limitations. In particular, Mn removal efficiency is expected to decrease due to permeability changes related to the dissolution-precipitation process and reduced interaction of fluids with fluorapatite surface linked to increasing Mn phosphate / fluorapatite ratio. Keeping those limitations in mind, it is estimated that based on the rate of Mn removal within the first 140 h in the batch experiments with initial fluid pH of 4–5 (and pH remaining $\leq$ 6 within the first 140 h reaction), 100 % Mn removal is predicted to occur within 24 days considering 100 mL of fluids and 200 mg of apatite in a flow system where pH remains $\leq$ 6. Upscaling those results to field scale treatment, considering a 1 m thick permeable barrier of natural fluorapatite with 40 % porosity and a flux of 0.04 $m^3 m^{-2} d^{-1}$, the barrier would be effective at removing 100 % Mn (of fluids containing up to 100 mg L^{-1} Mn) for at least about 3 years based on the conditions of our experiment, resulting in 0.4 % of the fluorapatite converted to Mn phosphate in that time period.

4.3. Chromium metal removal as a function of pH

Similar to the results from the Mn sulfate experiments, it is clear that the amount of Cr removed from solution within a certain time interval is greater for solutions with higher pH within the acid to neutral pH range studied (Fig. 8). Very minor Cr removal is achieved in the experiments with initial pH of 1.5 and 2.0. In contrast, all Cr is removed from solution within about 250 h in the solution with initial pH of 4.6. Removal of 78–95 % Cr is observed in the experiments with initial pH of 2.8, 3.3 and 3.4. Comparison of the Cr sulfate experiment with the Mn sulfate experiment for initial pH of 2.8 clearly indicates that Cr removal is achieved more rapidly than Mn removal under conditions of the same initial solution pH, because 56 % Cr versus 35 % Mn is removed within 400 h. In the experiment with both Cr sulfate and Mn sulfate, only Cr is removed from solution within 4 weeks, confirming the faster or preferential removal of Cr in comparison with Mn (Fig. 11). The starting pH of this Cr-Mn sulfate experiment is 3.7, and the pH does not reach a value of 5 within the duration of the experiment. The results from the experiments with Mn sulfate indicate that Mn phosphate formation only starts once the solution has reached a pH of 5 (Fig. 5). Hence, the fluid pH evolution during the experiment can explain the lack of Mn removal in the combined Cr-Mn sulfate experiment. For the Cr sulfate experiment with initial pH of 7.0, instant precipitation and Cr removal took place upon addition of NaOH to obtain the targeted neutral pH. It is interpreted that a chromium (hydr) oxide was formed instantly at those conditions.

PHREEQC geochemical modelling of the Cr sulfate experiments indicate that the distribution of the Ca species has a similar trend as that in the Mn sulfate experiments with Ca^{2+} becoming more dominant and $CaSO_4^{\circ}$ becoming less dominant in experiments with increasing initial pH (Fig. S2A). For Cr(III) species distribution, Cr^{3+} becomes less dominant, whereas $CrOH^{2+}$ and $Cr_3(OH)_4^{5+}$ become more dominant in experiments with increasing initial pH (Fig. S2B). $Cr(OH)_2^{+}$ becomes more important in experiments with higher initial pH, with up to 10 % of the Cr(III) species in the experiment with initial pH of 7.0. $Cr_2(OH)_2^{4+}$ also has a minor contribution with up to 2.6 % of the Cr(III) species in experiments with initial pH of 3.3 and 3.4 (Fig. S2B). The P (V) species distribution is dominated by H_3PO_4 and $H_2PO_4^{-}$, with decreasing contribution of the former and increasing contribution of the latter in experiments with increasing initial pH (Fig. S2C). In terms of saturation index, the solution in the experiment with initial pH of 1.5 is oversaturated with respect to gypsum and anhydrite, in contrast to the experiments with higher pH (Table S2). The solutions in experiments with initial pH of 2.0–7.0 are oversaturated with respect to Cr_2O_3 with higher saturation index in experiments with higher pH (Table S2).

The measured concentration of Cr lost from solution against Ca gained in solution indicates that in the experiment with initial pH of 4.6 a mole-per-mole exchange of Ca with Cr occurs in the fluorapatite structure (Fig. 15). This interpretation is supported by the fact that the P concentration remains very low in the solution ($\leq$ 0.2 mmol L^{-1}), in contrast to the increasing Ca concentration and decreasing Cr concentration, supporting that a new phosphate phase is being formed. The data are a bit more variable for the Cr experiments, in comparison with the Mn experiments. However, the trend line of the data indicate exchange of 1 mol of Ca by 1 mol of Cr in the precipitate. Exchange of Ca by Cr in apatite via a solid-state diffusion mechanism is very unlikely at the low temperature of 35 °C. This exchange of Ca for trivalent Cr is rather interpreted to result from a dissolution-precipitation mechanism, similar to that interpreted for divalent Mn. Based on the change in concentrations of Ca, Cr and P in solution, we have derived the stoichiometry of the phosphate precipitate to have a molar Cr/P ratio of 1.69 $\pm$ 0.06, assuming a Ca/P ratio of 1.67 in the starting material, or 1.79 $\pm$ 0.06, considering the measured Ca/P ratio of 1.77 in the apatite starting material in our calculations. Incorporation of trivalent Cr occupying the Ca positions in the crystal structure has been described for hydroxyapatite $[Ca_5(PO_4)_3OH]$ (Wakamura et al., 1997), and we

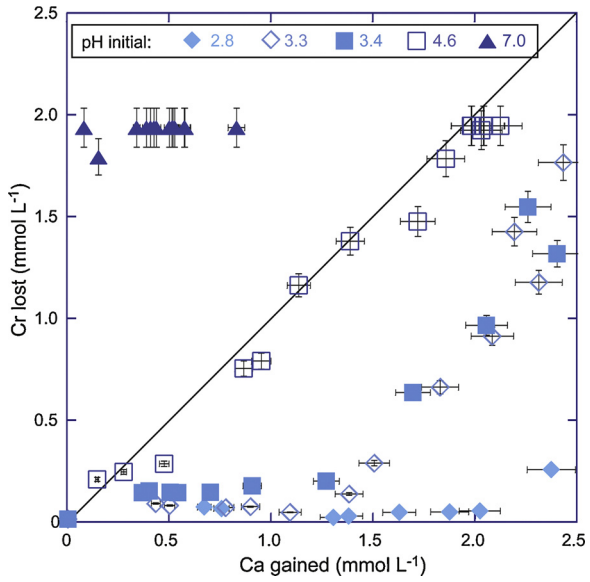

Fig. 15. Correlation of the concentration of Cr lost from solution against the concentration of Ca gained in the solution in the fluorapatite – Cr sulfate solution batch experiments with different initial pH.

propose that Cr incorporation can occur in a similar way in the fluorapatite crystal structure. The EPMA analysis confirms this with measurements on the very fine Cr-containing particles, with 6.1 ± 2.5 wt% Cr, 7.6 ± 1.8 wt% P and 10.6 ± 3.1 wt% Ca. We interpret that the EPMA measurements is affected by the resin and the very small nature of the particles, leading to a weight percentage that is underestimated, and relatively high uncertainty of the values. Nevertheless, we can derive the molar (Ca + Cr)/P ratio of the Cr-containing phase to be 1.6 ± 0.2, which is close to the stoichiometric Ca/P ratio of 5/3 in calcium fluorapatite, which may suggest the presence of $(Ca,Cr)_5(PO_4)_3F$ in our reaction products, rather than a potential $CrPO_4$ compound.

For the Cr sulfate experiments with initial pH of 3.3 and 3.4, initial fluorapatite dissolution-only occurs, as shown by the increase in Ca gained in solution without increase in Cr lost from solution, until a certain point, upon which both Ca gain and Cr loss start to increase in similar mole proportions (Fig. 15). This is also reflected in the Ca/P molar ratio which is stable at the start, and thereafter increases rapidly (Fig. 9). Very similar behaviour was observed in the Mn sulfate experiment with initial pH of 2.8. In the Cr sulfate experiments, Cr removal may be initiated after a fast pH increase at the start until a pH value of around 3.5 or 4, which then stabilizes. The link of Cr removal with pH confirms the interpretation of Cr removal by a dissolution-precipitation mechanism. Moreover, Cr removal is faster in the experiment with initial pH of 4.6 in comparison with those with initial pH of 2.8–3.4 (Fig. 8). The Cr removal rate seems to decrease with time in the experiment, along with a decrease in the Cr concentration in solution, and slight increase in pH.

These Cr batch reactor results demonstrate that natural fluorapatite is effective in removing Cr from waters with pH of 4–5. Keeping the additional complexity of flow through porous media in mind, it is estimated that based on the rate of Cr removal in the batch experiment with initial pH of 3.4, considering the time interval where pH = 4 (90–330 hours reaction time), 100 % Cr removal is predicted to occur within 19 days considering 100 mL of fluids and 200 mg of apatite in a flow system where pH remains constant at 4. Upscaling this to field scale treatment, considering a 1 m thick permeable reactive barrier containing natural fluorapatite (assuming 40 % porosity) and a water flux of 0.05 $m^3 m^{-2} d^{-1}$, the barrier would be effective at removing 100 % Cr (from fluids containing up to 100 mg L^{-1} Cr) for at least about three years based on our experimental data, resulting in 0.5 % of the fluorapatite converted.

5. Conclusions

Batch reactor experiments in this study have shown that the logarithm of the far-from-equilibrium dissolution rate of natural calcium fluorapatite is a linear function of solution pH. As a result of apatite dissolution in the acidic fluids, the pH increases during the experiment, and thus apatite has the capacity to neutralize acid mine drainage fluids. In the presence of divalent Mn or trivalent Cr in a sulfate matrix solution, exchange of Ca for Mn or Cr takes place in experiments with initial pH of around 4–5. This exchange is a result of a dissolution-precipitation mechanism, whereby apatite dissolves and a metal phosphate phase precipitates. In experiments with initial pH in the range of around 2.5–4, this exchange due to the dissolution-precipitation mechanism is preceded by a dissolution-only phase which causes an increase in the pH of the solution. The experiments demonstrate that heavy metal removal by apatite dissolution-precipitation mechanism is most effective in solutions with pH of 4–6. Removal of trivalent Cr is greater than that of divalent Mn from solution by use of apatite, considering similar pH and duration of the experiment. Removal of Cr is preferential to that of Mn from solutions that contain both metals in similar concentrations. The results in this study suggest that natural apatite is an inexpensive and promising material that can be used for passive remediation of contaminated soils and groundwater in arid regions that are subject to mining activities.

Author contributions

VV, CC, TH, RLG contributed to designing the research. CC and VV carried out most of the experiments and analyses. TH conducted the SEM-EDX analyses. JT conducted the NMR analyses. VV, CC, RLG, TH, JT contributed to interpretation of the results.

Declaration of Competing Interest

The authors declare no competing interests.

Acknowledgements

This research was funded by an EPSRC GCRF Institutional Sponsorship Award (EP/R512849/1). The UK 850 MHz solid-state NMR Facility used in this research was funded by EPSRC and BBSRC, as well as the University of Warwick including via part funding through Birmingham Science City Advanced Materials Projects 1 and 2 supported by Advantage West Midlands (AWM) and the European Regional Development Fund (ERDF). We would like to thank Mark Guyler for assistance with and maintenance of the ICP-OES and FTIR, and William Lewis and Stephen Argent for maintenance of the XRD in the School of Chemistry. The authors thank the Nanoscale and Microscale Research Centre (nmRC) for providing access to instrumentation and Elisabeth Steer for conducting the EPMA analyses in this study. We gratefully acknowledge the constructive and very helpful comments from the anonymous reviewers and the editorial handling by Dr. Navid Saleh, which improved this manuscript.

Appendix A. Supplementary data

Supplementary material related to this article can be found, in the online version, at doi:https://doi.org/10.1016/j.jhazmat.2020.122150.

References

Abdalla, F.A., Khalifa, I.H., 2013. Effects of phosphate mining activity on groundwater quality at Wadi Queh, Red Sea, Egypt. Arab. J. Geosci. 6, 1273–1282.

Al-Asheh, S., Banat, F., Mohai, F., 1999. Sorption of copper and nickel by spent animal bones. Chemosphere 39, 2087–2096.

Alexander, J.A., Zaini, M.A.A., Surajudeen, A., Aliyu, E.-N.U., Omeiza, A.U., 2019. Surface modification of low-cost bentonite adsorbents-A review. Part. Sci. Technol. 37, 534–545.

Alkattan, M., Oelkers, E.H., Dandurand, J.-L., Schott, J., 1997. Experimental studies of halite dissolution kinetics: I. The effect of saturation state and the presence of trace metals. Chem. Geol. 137, 201–219.

Amer, R., Ripperdan, R., Wang, T., Encarnacion, J., 2012. Groundwater quality and management in arid and semi-arid regions: case study, Central Eastern Desert of Egypt. J. Afr. Earth Sci. 69, 13–25.

Anawar, H.M., 2013. Impact of climate change on acid mine drainage generation and contaminant transport in water ecosystems of semi-arid and arid mining areas. Phys. Chem. Earth 58-60, 13–21.

Antonakos, A., Liarokapis, E., Leventouri, T., 2007. Micro-Raman and FTIR studies of synthetic and natural apatites. Biomaterials 28, 3043–3054.

Asere, T.G., Stevens, C.V., Du Laing, G., 2019. Use of (modified) natural adsorbents for arsenic remediation: a review. Sci. Total Environ. 676, 706–720.

Bishop, J.L., Lane, M.D., Dyar, M.D., King, S.J., Brown, A.J., Swayze, G.A., 2014. Spectral properties of Ca-sulfates: gypsum, bassanite, and anhydrite. Am. Mineral. 99, 2105–2115.

Chairat, C., Schott, J., Oelkers, E.H., Lartigue, J.-E., Harouiya, N., 2007. Kinetics and mechanism of natural fluorapatite dissolution at 25 degrees C and pH from 3 to 12. Geochim. Cosmochim. Acta 71, 5901–5912.

Chen, X., Wright, J.V., Conca, J.L., Peurrung, L.M., 1997a. Effects of pH on heavy metal sorption on mineral apatite. Environ. Sci. Technol. 31, 624–631.

Chen, X., Wright, J.V., Conca, J.L., Peurrung, L.M., 1997b. Evaluation of heavy metal remediation using mineral apatite. Water, Air Soil Pollut.Water Air Soil Pollut. 98, 57–78.

Chen, J.S., Yu, Z.W., Zhu, P.Z., Wang, J.F., Gan, Z.H., Wei, J., Zhao, Y.H., Wei, S.C., 2015. Effects of fluorine on the structure of fluorohydroxyapatite: a study by XRD, solid-state NMR and Raman spectroscopy. J. Mater. Chem. B 3, 34–38.

Cherniak, D.J., 2005. Uranium and manganese diffusion in apatite. Chem. Geol. 219, 297–308.

Chew, D.M., Spikings, R.A., 2015. Geochronology and thermochronology using apatite: time and temperature, lower crust to surface. Elements 11, 189–194.

Christoffersen, J., Christoffersen, M.R., 1982. Kinetics of dissolution of calcium hydroxyapatite V. The acidity constant for the hydrogen phosphate surface complex. J. Cryst. Growth 57, 21–26.

Cui, H., Fan, Y., Fang, G., Zhang, H., Su, B., Zhou, J., 2016. Leachability, availability and bioaccessibility of Cu and Cd in a contaminated soil treated with apatite, lime and charcoal: a five-year field experiment. Ecotoxicol. Environ. Saf. 134, 148–155.

Dominguez, M.I., Carpena, J., Borschnek, D., Centeno, M.A., Odriozola, J.A., Rose, J., 2008. Apatite and Portland/apatite composite cements obtained using a hydrothermal method for retaining heavy metals. J. Hazard. Mater. 150, 99–108.

Domínguez, M.I., Carpena, J., Borschnek, D., Centeno, M.A., Odriozola, J.A., Rose, J., 2008. Apatite and Portland/apatite composite cements obtained using a hydrothermal methods for retaining heavy metals. J. Hazard. Mater. 150, 99–108.

Dorozhkin, S.V., 2002. A review on the dissolution models of calcium apatites. Prog. Cryst. Growth Charact. Mater. 44, 45–61.

El Maghraby, A., 2012. Phosphate mining wastes at Abu Tartur Mine Area, Western Desert of Egypt. Aust. J. Basic Appl. Sci. 6, 231–248.

Embaby, A., Razack, M., Lecoz, M., Porel, G., 2016. Hydrogeochemical assessment of groundwater in the precambrian rocks, South Eastern Desert, Egypt. J. Water Resource Prot. 8, 293–310.

Fayiga, A.O., Ipinmoroti, M.O., Chirenje, T., 2018. Environmental pollution in Africa. Environ. Dev. Sustain. 20, 41–73.

Fedoroff, M., Jeanjean, J., Rouchaud, J.C., Mazerolles, L., Trocillier, P., Maireles-Torres, P., Jones, D.J., 1999. Sorption kinetics and diffusion of cadmium in calcium hydroxyapatites. Solid State Sci. 1, 71–84.

Fischer, C., Arvidson, R.S., Luttge, A., 2012. How predictable are dissolution rates of crystalline material? Geochim. Cosmochim. Acta 98, 177–185.

Fleet, M.E., Liu, X., 2003. Carbonate Apatite type A synthesized at high pressure: new space group and orientation of channel carbonate ion. J. Solid State Chem. 174, 412–417.

Fleet, M.E., Liu, X., 2004. Location of type B carbonate ion in type A-B carbonate Apatite synthesized at high pressure. J. Solid State Chem. 177, 3174–3182.

Fowler, B.O., 1974. Infrared studies of apatites. I. Vibrational assignments for calcium, strontium, and barium hydroxyapatites utilizing isotopic substitution. Inorg. Chem. 13, 194–207.

Gaft, M., Reisfeld, R., Panczer, G., Boulon, G., Shoval, S., Champagnon, B., 1997. Accommodation of rare-earths and manganese by apatite. Opt. Mater. 8, 149–156.

Gonzalez, V., Garcia, I., del Moral, F., de Haro, S., Sanchez, J.A., Simon, M., 2011. Impact of unconfined sulphur-mine waste on a semi-arid environment (Almeria, SE Spain). J. Environ. Manage. 92, 1509–1519.

Guidry, M.W., Mackenzie, F.T., 2003. Experimental study of igneous and sedimentary apatite dissolution: control of pH, distance from equilibrium, and temperature on dissolution rates. Geochim. Cosmochim. Acta 67, 2949–2963.

Han, H., Rafiq, M.K., Zhou, T., Xu, R., Masek, O., Li, X., 2019. A critical review of clay-based composites with enhanced adsorption performance for metal and organic pollutants. J. Hazard. Mater. 369, 780–796.

Harlov, D.E., 2015. Apatite: A fingerprint for metasomatic processes. Elements 11, 171–176.

Harouiya, N., Chairat, C., Kohler, S.J., Gout, R., Oelkers, E.H., 2007. The dissolution kinetics and apparent solubility of natural apatite in closed reactors at temperatures from 5 to 50 degrees C and pH from 1 to 6. Chem. Geol. 244, 554–568.

Harraz, H.Z., Hamdy, M.M., El-Mamoney, M.H., 2012. Multi-element association analysis of stream sediment geochemistry data for predicting gold deposits in Barramiya gold mine, Eastern Desert, Egypt. J. Afr. Earth Sci. 68, 1–14.

Hughes, J.M., 2015. The many facets of apatite. Am. Mineral. 100, 1033–1039.

Hughes, J.M., Rakovan, J.F., 2015. Structurally Robust, Chemically Diverse: Apatite and Apatite Supergroup Minerals. Elements 11, 165–170.

Hughes, J.M., Cameron, M., Crowley, K.D., 1989. Structural variations in natural F, OH, and Cl apatites. Am. Mineral. 74, 870–876.

Hughes, J.M., Cameron, M., Crowley, K.D., 1990. Crystal-structures of natural ternary apatities - solid-solution in the Ca5(PO4)3X (X=F, OH, Cl) system. Am. Mineral. 75, 295–304.

Jay, E.E., Rushton, M.J.D., Grimes, R.W., 2012. Migration of fluorine in fluorapatite - a concerted mechanism. J. Mater. Chem. 22, 6097–6103.

Kamiishi, E., Utsunomiya, S., 2013. Nano-scale reaction processes at the interface between apatite and aqueous lead. Chem. Geol. 340, 121–130.

Laurencin, D., Wong, A., Dupree, R., Smith, M.E., 2008. Natural abundance Ca-43 solid-state NMR characterisation of hydroxyapatite: identification of the two calcium sites. Magn. Reson. Chem. 46, 347–350.

Li, Z., Wang, F., Bai, T., Tao, J., Guo, J., Yang, M., Wang, S., Hu, S., 2016. Lead immobilization by geological fluorapatite and fungus Aspergillus niger. J. Hazard. Mater. 320, 386–392.

Luttge, A., Arvidson, R.S., Fischer, C., Kurganskaya, I., 2019. Kinetic concepts for quantitative prediction of fluid-solid interactions. Chem. Geol. 504, 216–235.

Ma, Q.Y., Traina, S.J., Logan, T.J., Ryan, J.A., 1993. In situ lead immobilization by apatite. Environ. Sci. Technol. 27, 1803–1810.

Ma, Q.Y., Logan, T.J., Traina, S.J., 1995. Lead immobilisation from aqueous solutions and contaminated soil using phosphate rocks. Environ. Sci. Technol. 29, 1118–1126.

Mansour, S.A., Sidky, M.M., 2003. Ecotoxicological Studies. 6. The first comparative study between Lake Qarun and Wadi EI-Rayan wetland (Egypt), with respect to contamination of their major components. Food Chem. 82, 181–189.

McCubbin, F.M., Jones, R.H., 2015. Extraterrestrial apatite: planetary geochemistry to astrobiology. Elements 11, 183–188.

Mouflih, M., Aklil, A., Sebti, S., 2005. Removal of lead from aqueous solutions by activated phosphate. J. Hazard. Mater. 119, 183–188.

Naz, A., Chowdhury, A., Mishra, B.K., Gupta, S.K., 2016. Metal pollution in water environment and the associated human health risk from drinking water: a case study of Sukinda chromite mine, India. Hum. Ecol. Risk Assess. 22, 1433–1455.

Oliva, J., De Pablo, J., Cortina, J.-L., Cama, J., Ayora, C., 2010. The use of Apatite IITM to remove divalent metal ions zinc(II), lead(II), manganese(II) and iron(II) from water in passive treatment systems: column experiments. J. Hazard. Mater. 184, 364–374.

Oliva, J., De Pablo, J., Cortina, J.-L., Cama, J., Ayora, C., 2011. Removal of cadmium, copper, nickel, cobalt and mercury from water by Apatite IITM: column experiments. J. Hazard. Mater. 194, 312–323.

Oliva, J., Cama, J., Cortina, J.L., Ayora, C., De Pablo, J., 2012. Biogenic hydroxyapatite (Apatite IITM) dissolution kinetics and metal removal from acid mine drainage. J. Hazard. Mater. 213-214, 7–18.

Peld, M., Tonsuaadu, K., Bender, V., 2004. Sorption and desorption of Cd2+ and Zn2+ ions in apatite-aqueous systems. Environ. Sci. Technol. 38, 5626–5631.

Pfeiffer, M., Batbayar, G., Hofmann, J., Siegfried, K., Karthe, D., Hahn-Tomer, S., 2015. Investigating arsenic (As) occurrence and sources in ground, surface, waste and drinking water in northern Mongolia. Environ. Earth Sci. 73, 649–662.

Piccirillo, C., Moreira, I.S., Novais, R.M., Fernandes, A.J.S., Pullar, R.C., Castro, P.M.L., 2017. Biphasic apatite-carbon materials derived from pyrolysed fish bones for effective adsorption of persistent pollutants and heavy metals. J. Environ. Chem. Eng. 5, 4884–4894.

Rakovan, J.F., Pasteris, J.D., 2015. A technological gem: materials, medical, and environmental mineralogy of apatite. Elements 11, 195–200.

Ross, S.D., 1974. Sulphates and other oxy-anions of group VI. In: Farmer, V.C. (Ed.), The Infrared Spectra of Minerals. The Mineralogical Society, London, pp. 423–444.

Ruby, M.V., Davis, A., Nicholson, A., 1994. In situ formation of lead phosphates in soils as a method to immobilize lead. Environ. Sci. Technol. 28, 646–654.

Salisbury, J.W., Walter, L.S., Vergo, N., D'Aria, D.M., 1991. Infrared (2.1-25 μm) Spectra of Minerals. John Hopkins University Press, Baltimore.

Shin, W., Kim, Y.-K., 2016. Stabilization of heavy metal contaminated marine sediments with red mud and apatite composite. J. Soils Sediments 16, 726–735.

Sivakumar, M.V.K., Das, H.P., Brunini, O., 2005. Impacts of present and future climate variability and change on agriculture and forestry in the arid and semi-arid tropics. Clim. Change 70, 31–72.

Sljivic-Ivanovic, M., Smiciklas, I., Milenkovic, A., Dojcinovic, B., Babic, B., Mitric, M., 2015. Evaluation of the effects of treatment factors on the properties of bio-apatite materials. J. Mater. Sci. 50, 354–365.

Smiciklas, I., Onjia, A., Raicevic, S., Janackovic, D., Mitric, M., 2008. Factors influencing the removal of divalent cations by hydroxyapatite. J. Hazard. Mater. 152, 876–884.

Stormer, J., Pierson, M.L., Tacker, R.C., 1993. Variation of F and Cl X-ray intensity due to anisotropic diffusion in apatite. Am. Mineral. 78, 641–648.

Valsami-Jones, E., Ragnarsdottir, K.V., Putnis, A., Bosbach, D., Kemp, A.J., Cressey, G., 1998. The dissolution of apatite in the presence of aqueous metal cations at pH 2-7. Chem. Geol. 151, 215–233.

Veado, M.A.R.V., Arantes, I.A., Oliveira, A.H., Almeida, M.R.M.G., Miguel, R.A., Severo, M.I., Cabaleiro, H.L., 2006. Metal pollution in the environment of Minas Gerais State - Brazil. Environ. Monit. Assess. 117, 157–172.

Viipsi, K., Sjoberg, S., Tonsuaadu, K., Shchukarev, A., 2013. Hydroxy- an fluroapatite as sorbents in Cd(II)-Zn(II) multi-component solutions in the absence/presence of EDTA. J. Hazard. Mater. 252-253, 91–98.

Wakamura, M., Kandori, K., Ishikawa, T., 1997. Influence of chromium(III) on the formation of calcium hydroxyapatite. Polyhedron 16, 2047–2053.

Wang, M., Wu, S., Guo, J., Zhang, X., Yang, Y., Chen, F., Zhu, R., 2019. Immobilization of cadmium by hydroxyapatite converted from microbial precipitated calcite. J. Hazard. Mater. 366, 684–693.
Webster, J.D., Piccoli, P.M., 2015. Magmatic apatite: a powerful, yet deceptive, mineral. Elements 11, 177–182.
Welch, S.A., Taunton, A.E., Banfield, J.F., 2002. Effect of microorganisms and microbial metabolites on apatite dissolution. Geomicrobiol. J. 19, 343–367.
Wooster, W.A., 1936. On the crystal structure of gypsum, CaSO4 2H(2)O. Z. Kristallogr. Cryst. Mater. 94, 375–396.
Xu, Y., Schwartz, F.W., 1994. Lead immobilisation by hydroxyapatite in aqueous solutions. J. Contam. Hydrol. 15, 187–206.
Xu, Y., Schwartz, F.W., Traina, S.J., 1994. Sorption of Zn2+ and Cd2+ on hydroxyapatite surfaces. Environ. Sci. Technol. 28, 1472–1480.
Young, E.J., Sheridan, D.M., Munson, E.L., 1966. Mineralogical notes - manganese- and strontium-bearing fluorpatite from Peerless Pegmatite South Dakota. Am. Mineral. 51 1516-&.
Zhu, Y., Zhang, X., Chen, Y., Xie, Q., Lan, J., Qian, M., He, N., 2009. A comparative study on the dissolution and solubility of hydroxylapatite and fluorapatite at 25 degrees C and 45 degrees C. Chem. Geol. 268, 89–96.
Zoheir, B.A., Akawy, A., 2010. Genesis of the abu marawat gold deposit, central Eastern Desert of Egypt. J. Afr. Earth Sci. 57, 306–320.
Zoheir, B., Moritz, R., 2014. Fluid evolution in the El-sid gold deposit, Eastern desert, Egypt. In: Garofalo, P.S., Ridley, J.R. (Eds.), Gold-Transporting Hydrothermal Fluids in the Earth'S Crust, pp. 147–175.